Stability of Polar Vortex Lattice in Ferroelectric Superlattices

Zijian Hong,[*,†] Anoop R. Damodaran,[‡] Fei Xue,[†] Shang-Lin Hsu,[‡,§,∥] Jason Britson,[†] Ajay K. Yadav,[‡,§] Christopher T. Nelson,[‡,§] Jian-Jun Wang,[†] James F. Scott,[⊥] Lane W. Martin,[‡,§] Ramamoorthy Ramesh,[*,‡,§,∥] and Long-Qing Chen[*,†]

[†]Department of Materials Science and Engineering, The Pennsylvania State University, University Park, Pennsylvania 16802, United States

[‡]Department of Materials Science and Engineering, University of California, Berkeley, California 94720, United States

[§]Materials Sciences Division, Lawrence Berkeley National Laboratory, Berkeley, California 94720, United States

[∥]Department of Physics, University of California, Berkeley, California 94720, United States

[⊥]Schools of Chemistry and Physics, University of St Andrews, St Andrews KY16 9ST, U.K.

S *Supporting Information*

ABSTRACT: A novel mesoscale state comprising of an ordered polar vortex lattice has been demonstrated in ferroelectric superlattices of $PbTiO_3/SrTiO_3$. Here, we employ phase-field simulations, analytical theory, and experimental observations to evaluate thermodynamic conditions and geometric length scales that are critical for the formation of such exotic vortex states. We show that the stability of these vortex lattices involves an intimate competition between long-range electrostatic, long-range elastic, and short-range polarization gradient-related interactions leading to both an upper and a lower bound to the length scale at which these states can be observed. We found that the critical length is related to the intrinsic domain wall width, which could serve as a simple intuitive design rule for the discovery of novel ultrafine topological structures in ferroic systems.

KEYWORDS: *Ferroelectric superlattices, ultrafine polar vortex, geometric length scale, phase-field simulations, topological structures by design*
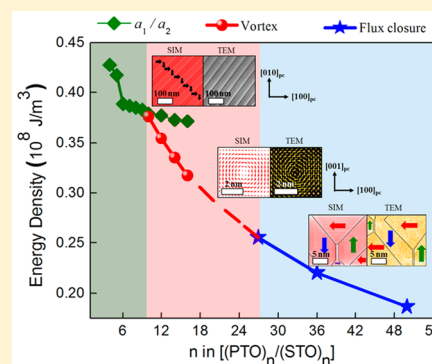
Artificial superlattices consisting of repeating layers of multiple solids have attracted broad attention within the solid-state community.[1−12] They offer additional degrees of freedom (beyond conventional "strain engineering") by which one can design multifunctional thin-film materials, wherein unit cells of combinations of solid materials are periodically stacked, often giving rise to novel emergent phenomena.[6−8] Within the realm of complex ferroelectric oxides, for instance in $PbTiO_3$/ $SrTiO_3$ (PTO/STO) superlattices, various novel phenomena and polar domain states have been observed (e.g., "improper ferroelectricity" appears in short period superlattices;[10,11] ordered vortex arrays form in intermediate period super-lattices;[12] and flux-closure domain structures exist in PTO/ STO multilayers and large period superlattices;[13] etc.). These states arise from complex interplay of competing energies, including depolarization, polarization/chemical gradients, long-range elastic interactions, and interfacial coupling, which dominate at different length scales and thus produce such exotic thickness-dependent ground states.[9,14]

A vortex is an intriguing topological structure, which attracts broad attention in the scientific community from various perspectives, including polar vortices in meteorology and astronomy, vortex flow in fluid mechanics, spin spirals and skyrmions in ferromagnetics, etc. Ferroelectric vortex states (characterized by the continuous rotation of ferroelectric polarization around a vortex core, and analogous to those found in magnetic systems) have been theoretically predicted in ferroelectric nanoparticles and nanodots (often termed "zero-dimensional ferroelectrics"[15−22]), nanoplatelets,[23] nanosheets,[24] nanotube[25] and superlattices,[11,26] but long-range vortex ordering has not been deterministically isolated in experiments. A breakthrough was recently achieved in superlattices of $(PTO)_n/$ $(STO)_n$ on $DyScO_3$ (DSO) $(110)_o$ substrates which exhibit ordered arrays of vortices for intermediate values of n (∼10− 16, number of unit cells).[12] Along with the excitement for emergent functionalities in these vortex states and their technological implications, a number of fundamental questions arise regarding their origin and thermodynamic stability. In this work, we explore the following questions: (1) What are the chemical, electrostatic, and mechanical boundary conditions that promote the formation of such a vortex lattice in ferroelectric superlattices? (2) What is the length scale at which the vortex lattice is stable over competing ferroelectric
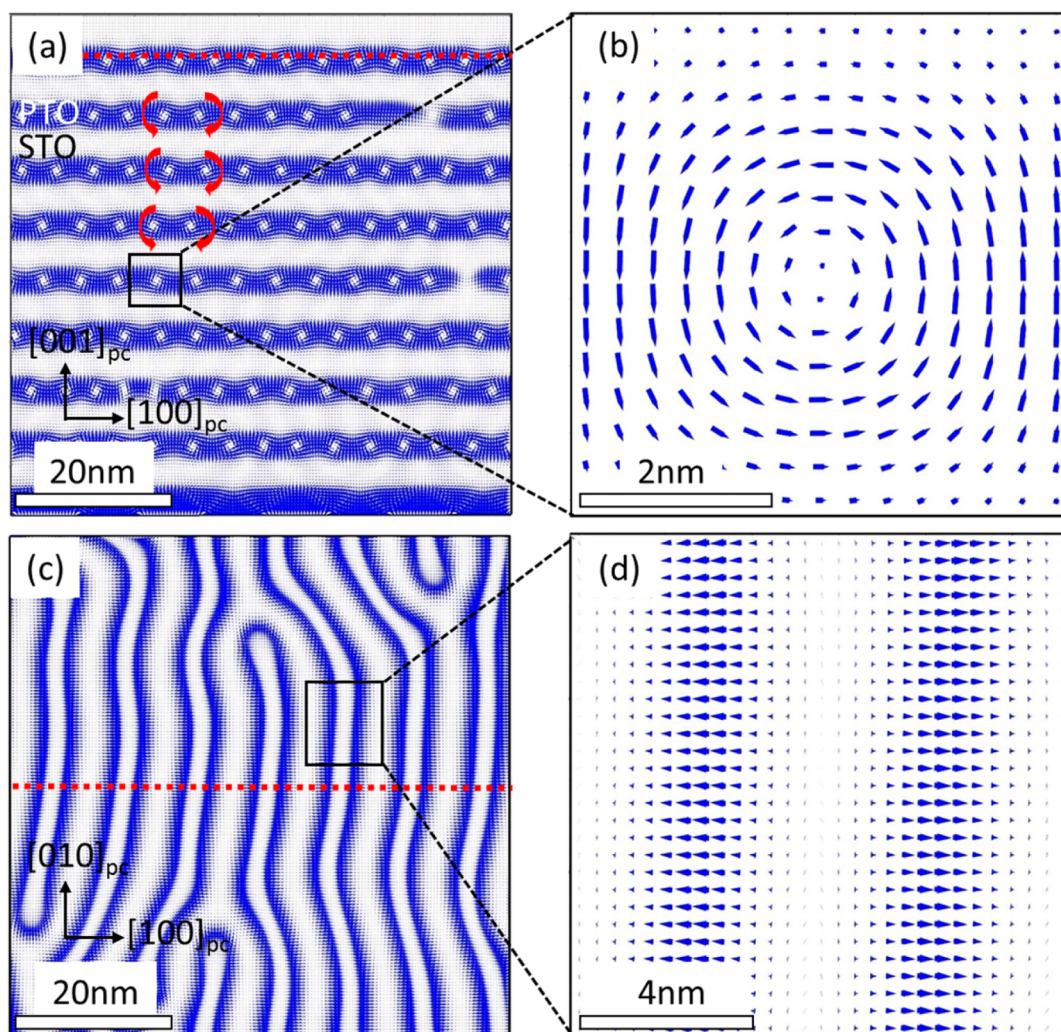
Figure 1. Polarization vector maps for vortices in the $(PTO)_{10}/(STO)_{10}$ superlattice system, calculated from a phase-field simulation. (a) Spatial distribution of polarization in the cross-section $(010)_{pc}$ plane, showing the vortex structures. (b) Zoom-in result for a single vortex showing the continuous rotation of the polarization vector. (c) Planar view of the PTO layer, showing vortex line arrangement. (d) Zoom-in of the vortex line. Dotted lines in panels a and c show the planes where the planar view and cross-sectional view are plotted, respectively.

states? (3) What is the role of the STO layers, and how can we engineer new phases by tuning these layers?

To address these questions, we employ phase-field modeling in conjunction with a Ginzburg–Landau based analytical model to explore the stability of the vortex structure as a function of superlattice periodicity and STO layer thickness. Over the last two decades, phase-field modeling has been widely employed to study the domain structure and evolution in ferroelectric thin films[27−30] and has also been successfully extended to unveil the domain structures, switching kinetics, phase diagrams, and physical properties for a variety of superlattice systems.[31−33] In the phase-field approach, the spatially dependent polarization vector $\vec{P} = (P_x, P_y, P_z)$ is selected as the order parameter to describe the polar states. The evolution of this polarization is governed by the time-dependent Ginzburg–Landau (TDGL) equations and driven by the minimization of the total energy, which is comprised of chemical, elastic, electric, and polarization gradient energies.[28] An iterative perturbation method is adopted to accommodate for the elastic anisotropy and inhomogeneity of the PTO and STO layers when solving the mechanical equilibrium equations.[34] The short-circuit electric boundary condition is applied at the top surface of the

superlattice film and the film/substrate interface. A thin-film mechanical boundary condition is used, where the top surface of the superlattice film is assumed to be stress free while the displacement at the substrate bottom sufficiently far from the film/substrate interface is fixed to zero.[27] The calculation details, as well as the related parameters, can be found in the literature[27,35−39] and are further explained in the Supporting Information.

We start by exploring the phase-field simulation results for a $(PTO)_{10}/(STO)_{10}$ superlattice coherently strained to a DSO $(110)_o$ substrate, a model system that has demonstrated ordered vortex arrays in previous experiments.[12] The pseudocubic lattice parameters of PTO and STO are set as 3.957 and 3.905 Å, respectively,[35,36] while the anisotropic in-plane lattice constants for DSO are set as 3.952 and 3.947 Å[38] to determine the effective substrate strain. It is easily seen that the calculated polarization distribution (Figure 1a) in the PTO layers mimics the ordered vortex lattice. The zoom-in of a single vortex in the PTO layer clearly shows the continuous rotation of polarization vectors surrounding the vortex center (Figure 1b), which is experimentally confirmed by the high-resolution transmission electron microscopy (HRTEM)

mapping of polar vectors (see ref 12 and the Supporting Information). Both the simulation and experimental results indicate that the size of each vortex is 4−5 nm for this particular superlattice periodicity. We also note that in contrast to the flux-closure polarization structures,[13,40−42] where abrupt polarization changes occur only near the distinct domain wall area, the vortex structures exhibit a continuously rotating polarization. The vortex state is distinctly different and represents a highly inhomogeneous polarization mode that is characterized by a one-dimensional singularity at the vortex core as against two-dimensional domain walls that appear in the flux-closure structures. The vortex core structure in the ferroelectric system is unique as compared to the topologically protected vortex core in magnetic systems where the magnitude of polarization exhibits a huge decrease near the core due to the strong anisotropy in the ferroelectric system. Furthermore, a planar section (Figure 1c) of the PTO layer reveals that the vortices form long chains along the axial direction, often intersecting other vortices in a classic dislocation-like pattern, in excellent agreement with planar section TEM studies.[12] A magnified view of this planar section (Figure 1d) shows the in-plane polarization of neighboring vortices pointing tail-to-tail and separated by an out-of-plane polarization region confirming the antirotation relationship between neighboring vortex pairs throughout the axial direction.

To find the intrinsic thermodynamic stability region for the vortex states, we analytically predict the emergence of the vortex states following references[43−45] using a simplified two-dimensional (2D) model. The local free energy of the $x−z$ 2D system can be written as

$$F = \int \left\{ a_1 P_x^2 + a_3 P_z^2 + a_{11} P_x^4 + a_{33} P_z^4 + a_{12} P_x^2 P_z^2 \right.$$
$$+ a_{111}(P_x^6 + P_z^6) + a_{112}(P_x^4 P_z^2 + P_x^2 P_z^4)$$
$$+ g_0 / 2 \left[\left(\frac{\partial P_x}{\partial x}\right)^2 + \left(\frac{\partial P_x}{\partial z}\right)^2 + \left(\frac{\partial P_z}{\partial x}\right)^2 + \left(\frac{\partial P_z}{\partial z}\right)^2 \right]$$
$$\left. - \frac{1}{2}\varepsilon_0 \varepsilon_{11} E_x^2 - \frac{1}{2}\varepsilon_0 \varepsilon_{33} E_z^2 - E_x P_x - E_z P_z \right\} dx \, dz$$

$$\tag{1}$$

where the a-parameters are the modified Landau coefficients under the thin-film boundary condition;[46] g_0 is the isotropic gradient energy coefficient; E_x and E_z are the x and z components of the local electric field, respectively (which is composed of externally applied field and depolarization field). ε_{11} and ε_{33} are the background dielectric constants. The mechanical effects are effectively included in the modified Landau coefficients through the thin-film boundary condition. Minimizing the total free energy with respect to P_x and P_z, one can deduce

$$2a_1 P_x + 4a_{11} P_x^3 + 2a_{12} P_x P_z^2 + 6a_{111} P_x^5$$
$$+ a_{112}(4P_x^3 P_z^2 + 2P_x P_z^4) - g_0 \left(\frac{\partial^2 P_x}{\partial x^2} + \frac{\partial^2 P_x}{\partial z^2} \right) = E_x$$

$$\tag{2}$$

$$2a_3 P_z + 4a_{33} P_z^3 + 2a_{12} P_z P_x^2 + 6a_{111} P_z^5$$
$$+ a_{112}(4P_z^3 P_x^2 + 2P_z P_x^4) - g_0 \left(\frac{\partial^2 P_z}{\partial x^2} + \frac{\partial^2 P_z}{\partial z^2} \right) = E_z$$

$$\tag{3}$$

where the curl of the electric field is zero because no magnetic field is involved:

$$\frac{\partial E_x}{\partial z} = \frac{\partial E_z}{\partial x}$$

$$\tag{4}$$

The electrostatic equilibrium is

$$\varepsilon_0 k_{11} \frac{\partial E_x}{\partial x} + \varepsilon_0 k_{33} \frac{\partial E_z}{\partial z} = -\left(\frac{\partial P_x}{\partial x} + \frac{\partial P_z}{\partial z} \right)$$

$$\tag{5}$$

In the vicinity of the vortex core, one can explicitly deduce a relationship between the vortex aspect ratio r (ratio of vortex in-plane size, d, to the superlattice periodicity, a_f) and the superlattice periodicity (see the Supporting Information):

$$\frac{1}{r^2} + 1 = \frac{a_f^2}{a_0^2}$$

$$\tag{6}$$

where a_0 is the "characteristic length" related to the gradient energy coefficients and the modified Landau coefficients, which can also be estimated by the width of the 180° domain wall δ, $a_0 \sim \pi\delta/\sqrt{2}$ (Supporting Information). At room temperature, for short period PTO/STO superlattices, a rough estimation gives a value of ~3.2 nm for the "characteristic length". Since the shape of the vortex is largely controlled by the aspect ratio r, we plot it as a function of superlattice periodicity (Figure 2). It
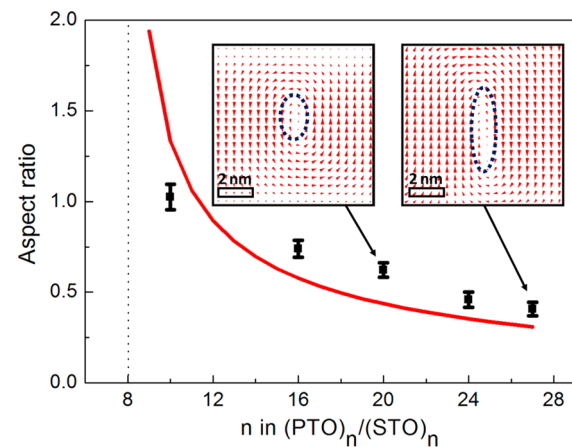
Figure 2. "Vortex" aspect ratio as a function of superlattice periodicity. The red curve is calculated according to eq 6, where a value of 8 unit cells is used for a_0. The square data points and error bars are results calculated from phase-field simulations. The left and right insets are the simulated domain structures for $(PTO)_{20}/(STO)_{20}$ and $(PTO)_{27}/(STO)_{27}$, respectively. The dashed line shows criterion 7. The vortex core is highlighted with a dotted ellipse which shows the elongation and the decrease of the aspect ratio with increasing superlattice periodicity n.

can be seen that the aspect ratio decreases with increasing periodicity from both eq 6 and the phase-field simulation results. Compared with the vortex patterns in $(PTO)_{10}/(STO)_{10}$ superlattices (Figure 1b,c), the vortex cores in $(PTO)_{20}/(STO)_{20}$ (left inset, Figure 2) are more elongated along the thickness direction than those in $(PTO)_{10}/(STO)_{10}$,

and it further elongates to resemble a classic 180° domain wall in a $(PTO)_{27}/(STO)_{27}$ superlattice (right inset, Figure 2). The elongation of the vortex core with increasing size has also been captured experimentally by TEM polar mapping of $(PTO)_{16}/$ $(STO)_{16}$ superlattice and was shown in previous two-dimensional phase-field simulations.[47] This comparison gives general good agreements between the analytical estimates (which partly ignored the complexity of the model system and originated from a simple quasi 2D model) and the phase-field simulations (which takes full consideration of the strain inhomogeneity and complex polar structure formation), which validates this relatively simple analytical model.

On the basis of eq 6, to ensure a physical solution (the square of aspect ratio r must not be negative) for the vortex state, a_f and a_0 must satisfy

$$a_f \geq a_0 \qquad (7)$$

Correspondingly, for superlattice periodicities where $a_f < a_0$ (i.e., for $n \leq 8$), the vortex state is unstable and inplane domains form. The upper bound for the vortex lattice is obscure because of the continuous nature of the vortex to flux-closure transition, and we can only estimate the critical aspect ratio of $r \sim 0.3$, below which the circular vortex core becomes a classic 180° type domain wall based on the phase-field simulation results given in the insets of Figure 2. The condition for stabilizing the vortex structure can be derived by combining the lower boundary from eq 7 and the upper boundary by substituting $r = 0.3$ to eq 6:

$$a_0 \leq a_f \leq \sqrt{12}\, a_0 \qquad (8)$$

Practically, the smooth circular-like rotation pattern can be expected where

$$a_f \sim \sqrt{2}\, a_0 \sim \pi\delta \qquad (9)$$

Equations 8 and 9 give the condition on the range of superlattice periodicity for which vortex structure may be expected. In order to observe a nanoscale vortex structure, the "characteristic length" a_0, which can be estimated by the 180° domain wall width of the bulk crystal, should be some intermediate value. If it is too small, the stability window given by eq 8 will be too small so that this structure cannot be captured experimentally. On the other hand, a large a_0 leads to an increase in the threshold transition length where dramatic increase in the polarization rotation region would lead to a large increase in gradient energy, which will favor the simple a/c-type structure. It is worth noting that eq 8 bridges the stability of mesoscale vortex with intrinsic bulk ferroelectric material properties (i.e., domain wall width) that serves as an intuitive simple design rule for the discovery of vortex and other possible topological structures. It is also found that this rule not only works well for the current PTO/STO system and other low-dimensional PTO nanostructures but also serves as a generally good estimate for the length scale of vortex or vortexlike structures in other ferroelectric materials, e.g., $BaTiO_3$ (see refs 48 and 49 for the sizes of the vortex or vortexlike structure in rhombohedral and orthorhombic phases; the domain wall width is given by ref 50) and $BiFeO_3$ (see ref 51 for the size of vortexlike structure and ref 52 for the domain wall width).

The temperature effect can also be described by eq 6. With increasing temperature, the "characteristic length" increases, giving rise to an upward shift of the phase boundary between the a_1/a_2 twin domains and vortex states. As a result, for a given periodicity, e.g., $(PTO)_{16}/(STO)_{16}$, a phase transition from

vortex to a_1/a_2 twins can be expected when temperature increases; such temperature-dependent phase transition was found by recent experimental results. Further reduction in the aspect ratio also indicates a lowering of symmetry, which is equivalent to the decrease in the k value as shown in Lukyanchuk et al., where the shape of the polarization domain changes from polyhedron-like to triangular-like.[53]

To better understand the nature of length-scale effects, we explored the evolution of the polar state of the PTO layer as a function of superlattice periodicity through integrated computational−experimental observations. As revealed in Figure 3, with
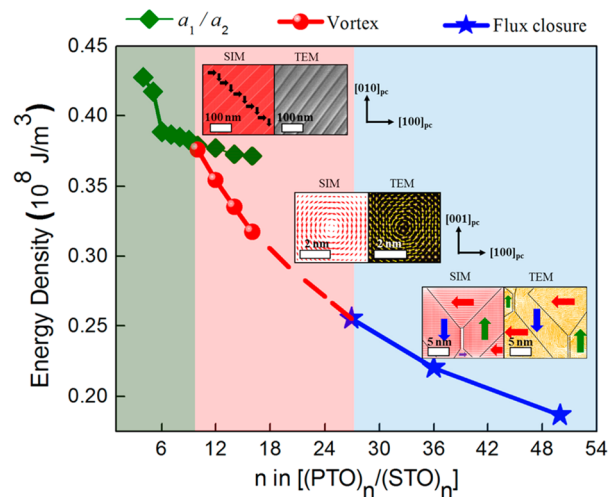

Figure 3. Phase diagram and total energy density for the $(PTO)_n/$ $(STO)_n$ superlattice grown on the DSO substrate, as calculated by the phase-field simulations and verified experimentally. Insets: The top left shows the simulation and planar TEM result of in-plane view of a_1a_2 twin-domain structure for $n = 6$. The middle left and right are the vortex structure for $n = 10$ from simulation and experimental TEM mapping, respectively. The bottom left and right insets are the cross sections of flux-closure structure for $n = 50$ from phase-field simulation and experimental TEM vector mapping, respectively. "SIM" and "TEM" stand for simulation and transmission electron microscopy data, respectively.

increasing superlattice period, the total energy density of the lowest energy state decreases monotonically. The higher total energy density at lower superlattice periodicity is related to the decreased benefits from the Landau energy and is indicative of a decreased stability of the ferroelectric state. In this regime of length scales (up to $n = 10$), strong depolarization effects drive the system into a completely in-plane polarized ferroelectric $a_1/$ a_2 twin-domain structure (top left inset, Figure 3) over the elastically preferred c/a domain structure (corresponding to the domain structure observed in thick PTO film under strain condition from the DSO $(110)_o$ substrate[54]), as revealed by both phase-field simulation and planar and cross-sectional TEM (Supporting Information). At the superlattice period $n \geq 10$ (length scale of ~ 4 nm), the formation of vortex states becomes feasible because of the lowering of the Landau and elastic energy density even at the expense of increased gradient energy contributions. This sets the lower-bound for the observation of vortex states in the system. Consequently, for superlattice period $n \geq 10$, it adopts ordered configurations that involve an intimate balance among long-range elastic and electrostatic, as well as short-range polarization gradient effects. Thus, with increasing period from $n \approx 10$ to $n \approx 16$, we see that

the vortex state (middle inset, Figure 3) becomes favorable, and we predict a phase transition from the in-plane polarized a_1/a_2 ferroelectric phase to an ordered vortex lattice. On the other hand, the transition from a vortex to a flux-closure domain structure (bottom inset, Figure 3) at large superlattice periodicity is continuous and a more subtle one.

From the energy point of view, the formation of a vortex at short-to-intermediate periods (e.g., $n \approx 10$ to $n \approx 16$) can be understood as a result of a balance between the individual energies: the combined effect of elastic and electric energies favors mixtures of in-plane and out-of-plane polarization, whereas the gradient energy is lower in the smooth rotating configuration (i.e., vortex) as compared to the structure with distinct domain walls (e.g., flux-closure) at short periods. The higher gradient energy in the flux-closure compared to vortex at lower periods can be understood, because the gradient energy density is much larger near the conventional domain walls (e.g., 180° and 90° walls in the tetragonal system) as compared to the smooth polarization rotation pattern in a vortex structure.

To further explore the role of the insulating STO layers, a phase diagram with varying STO layer thickness (i.e., $(PTO)_{10}/(STO)_m$) and the analysis of the electric energy density of the two layers are calculated by the phase-field method, as shown in Figure 4. With thin STO layers (e.g., $m = 2$) between the PTO
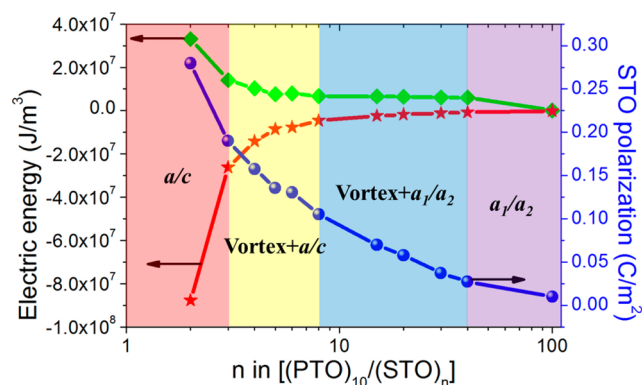
Figure 4. Phase diagram, STO polarization, and average electric energy density for the $(PTO)_{10}/(STO)_n$ superlattice grown on a DSO substrate, as calculated using phase-field simulations, showing the existence of a/c, vortex mixtures, and a_1/a_2.

layers, STO is highly polarized by the PTO layers because of the large internal field. As a consequence, the electric energy density inside the STO layer is highly negative because the internal electric field and polarization is in the same direction in this layer. Meanwhile, the electric energy density of PTO layers are highly positive with thin STO layers due to the depolarization effect, where the internal field in these layers are in the opposite direction with polarization. The significant polarization inside the STO layers serves as the bridge that connects the PTO layers; hence, an a/c twin structure forms, similar to the domain pattern for a PTO thin film grown on a DSO substrate, which forms to lower the elastic energy of the PTO layers. The polar phase of STO has been observed recently in both experiment and theory with a polarization up to 0.3 C/m^2 in ultrathin films.[55] Upon increasing the STO layer thickness, there is a monotonic decrease in the average polarization as well as in the internal field inside the STO layer, which decreases the magnitude of the electric energy density of the STO layers. In order to decrease the polar

discontinuity at the interface, the vortex states are formed. The vortex state is often mixed with other states (e.g., a/c with thin STO layers while a_1/a_2 at thick STO layers) to reduce the elastic and electric energies. With increasing of the STO layer thickness m, it is expected that the vortex ratio increases, which decreases the polar discontinuity at the PTO/STO interface as well as the electric energy density of the PTO layers. As the STO layer thickness increases further, the polarization in the STO layers vanish, which will eventually lead to the formation of a_1/a_2 twin structure in an attempt to further reduce the electric and gradient energy of the PTO layer at the expense of increased elastic energy.

Ultimately, the importance of the STO layers can be addressed as follows: the polarizability of these layers could be used to tune the polar discontinuity as well as the strength of the depolarization field, in combination with the size effect. The stability of the ground-state polar vortex phase is strongly influenced by the magnitude of polarization in these layers, the variation of which could lead to a rich phase diagram. In general, a less polarizable intermediate layer with smaller polarization leads to a completely in-plane polarization state (i.e., a_1/a_2) in the PTO layers to decrease the polar discontinuity at the interface and the electric energy of the system. A larger polarization in the intermediate layers leads to the formation of polarization states containing out-of-plane domains (i.e., a/c and even c^+/c^-). Indeed, a recent experimental observation showed the transition from c-like domains with polarization curling to mixed c/a-like domains in an ultrathin PTO film with a bottom LSMO electrode, primarily due to the increase in the depolarizing strength for thinner films with incomplete electrode screening.[56] Thus, it might be more feasible to choose weak ferroelectrics instead of a purely paraelectric material to design tunable domain structures and properties by engineering the thickness or composition of these layers.

In summary, we established that polar vortex lattices can be stabilized at intermediate length scales in a paraelectric/ferroelectric superlattices by manipulating the electrical, chemical, and mechanical energy contributions. On the basis of a simple analytical estimate and phase-field simulations, we provide a design rule to help identify the theoretical stability range for the vortex lattices. The role of each individual energy contribution in the formation of a vortex state is studied by calculating a size-dependent phase diagram. For the PTO/STO superlattice grown on a $(110)_o$-DSO substrate, it is shown that elastic energy favors out-of-plane polarization of the superlattice while the electric energy (in particular the depolarization energy) tries to keep polarization in-plane. Meanwhile, electric energy prefers a small spatial spacing between the vortices as well as large thickness of the ferroelectric layers, whereas the polarization gradient energy favors uniform polarization or smooth polarization rotation and thus large spacing between vortices. These competing interactions lead to a transition from a_1/a_2 twin polar states, to vortex lattice, and eventually to flux-closure lattices with increasing superlattice periodicity. The role of STO layers is further explored within the $(PTO)_{10}/(STO)_n$ phase diagram, indicating that the tunable depolarizing strength can help engineer multiple phases, and the existence of a weak ferroelectricity in the STO layer facilitates the formation of the vortex lattice. The calculated phase diagrams with various phases further suggest the possibility to switch between vortex and other phases under external stimuli, which might be of great importance in the design of next-generation electronic

devices. Thus, our work not only contributes to the further understanding of polar domain formation mechanism in current (PTO)/(STO) superlattice systems but also stimulates future studies on developing superlattice-based novel material systems.

■ AUTHOR INFORMATION

Corresponding Authors

*Z.H.: e-mail, zxh121@psu.edu.
*R.R.: e-mail, rramesh@berkeley.edu.
*L.-Q.C.: e-mail, lqc3@psu.edu.

ORCID Ⓘ

Zijian Hong: 0000-0002-3491-0884
Ajay K. Yadav: 0000-0001-5088-6506

Notes

The authors declare no competing financial interest.

■ REFERENCES

(1) Esaki, L.; Chang, L. *Phys. Rev. Lett.* **1974**, *33*, 495.
(2) Chowdhury, I.; Prasher, R.; Lofgreen, K.; Chrysler, G.; Narasimhan, S.; Mahajan, R.; Koester, D.; Alley, R.; Venkatasubramanian, R. *Nat. Nanotechnol.* **2009**, *4*, 235−238.
(3) Smadici, S.; Abbamonte, P.; Bhattacharya, A.; Zhai, X.; Jiang, B.; Rusydi, A.; Eckstein, J.; Bader, S.; Zuo, J. *Phys. Rev. Lett.* **2007**, *99*, 196404.
(4) Sinsheimer, J.; Callori, S. J.; Bein, B.; Benkara, Y.; Daley, J.; Coraor, J.; Su, D.; Stephens, P.; Dawber, M. *Phys. Rev. Lett.* **2012**, *109*, 167601.
(5) Lee, H.; Christen, H.; Chisholm, M.; Rouleau, C.; Lowndes, D. *Nature (London, U. K.)* **2005**, *433*, 395.
(6) Dawber, M.; Lichtensteiger, C.; Cantoni, M.; Veithen, M.; Ghosez, P.; Johnston, K.; Rabe, K.; Triscone, J. *Phys. Rev. Lett.* **2005**, *95*, 177601.
(7) Dawber, M.; Stucki, N.; Lichtensteiger, C.; Gariglio, S.; Ghosez, P.; Triscone, J. *Adv. Mater.* **2007**, *19*, 4153.
(8) Schlom, D.; Chen, L.; Fennie, C.; Gopalan, V.; Muller, D.; Pan, X.; Ramesh, R.; Uecker, R. *MRS Bull.* **2014**, *39* (02), 118−130.
(9) Stephanovich, V.; Luk'yanchuk, I.; Karkut, M. *Phys. Rev. Lett.* **2005**, *94*, 047601.
(10) Bousquet, E.; Dawber, M.; Stucki, N.; Lichtensteiger, C.; Hermet, P.; Gariglio, S.; Triscone, J.; Ghosez, P. *Nature (London, U. K.)* **2008**, *452*, 732.
(11) Aguado-Puente, P.; Junquera, J. *Phys. Rev. B: Condens. Matter Mater. Phys.* **2012**, *85*, 184105.
(12) Yadav, A.; Nelson, C.; Hsu, S.; Hong, Z.; Clarkson, J.; Schlepüetz, C.; Damodaran, A.; Shafer, P.; Arenholz, E.; Dedon, L.; Chen, D.; Vishwanath, A.; Minor, A.; Chen, L.; Scott, J.; Martin, L.; Ramesh, R. *Nature (London, U. K.)* **2016**, *530*, 198−201.
(13) Tang, Y.; Zhu, Y.; Ma, X.; Borisevich, A.; Morozovska, A.; Eliseev, E.; Wang, W.; Wang, Y.; Xu, Y.; Zhang, Z.; Pennycook, S. *Science* **2015**, *348*, 547−551.
(14) Balakrishna, A.; Huber, J. *Appl. Phys. Lett.* **2015**, *106*, 092906.
(15) Prosandeev, S.; Ponomareva, I.; Naumov, I.; Kornev, I.; Bellaiche, L. *J. Phys.: Condens. Matter* **2008**, *20*, 193201.
(16) Naumov, I.; Bellaiche, L.; Fu, H. *Nature (London, U. K.)* **2004**, *432*, 737.
(17) Aguado-Puente, P.; Junquera, J. *Phys. Rev. Lett.* **2008**, *100*, 177601.
(18) Sichuga, D.; Bellaiche, L. *Phys. Rev. Lett.* **2011**, *106*, 196102.
(19) Rodriguez, B.; Gao, X.; Liu, L.; Lee, W.; Naumov, I.; Bratkovsky, A.; Hesse, D.; Alexe, M. *Nano Lett.* **2009**, *9* (3), 1127−1131.
(20) Lee, B.; Nakhmanson, S.; Heinonen, O. *Appl. Phys. Lett.* **2014**, *104* (26), 262906.
(21) Gregg, J. *Ferroelectrics* **2012**, *433*, 74−87.
(22) Wang, J. *Appl. Phys. Lett.* **2010**, *97* (19), 192901.
(23) Chen, W.; Zheng, Y.; Wang, B. *Sci. Rep.* **2012**, *2*, 796.
(24) Chen, W.; Zheng, Y.; Wang, B. *Appl. Phys. Lett.* **2012**, *100* (6), 062901.
(25) Wang, J.; Kamlah, M. *Phys. Rev. B: Condens. Matter Mater. Phys.* **2009**, *80* (1), 012101.
(26) Aguado-Puente, P.; García-Fernández, P.; Junquera, J. *Phys. Rev. Lett.* **2011**, *107*, 217601.
(27) Li, Y.; Hu, S.; Liu, Z.; Chen, L. *Acta Mater.* **2002**, *50*, 395−411.
(28) Chen, L. *J. Am. Ceram. Soc.* **2008**, *91*, 1835−1844.
(29) Hong, Z.; Britson, J.; Hu, J.; Chen, L. *Acta Mater.* **2014**, *73*, 75−82.
(30) Wu, C.; Chen, W.; Zheng, Y.; Ma, D.; Wang, B.; Liu, J.; Woo, C. *Sci. Rep.* **2014**, *4*, 3946.
(31) Tian, W.; Jiang, J.; Pan, X.; Haeni, J.; Li, Y.; Chen, L.; Schlom, D.; Neaton, J.; Rabe, K.; Jia, Q. *Appl. Phys. Lett.* **2006**, *89* (9), 092905.
(32) Wu, P.; Ma, X.; Li, Y.; Gopalan, V.; Chen, L. *Appl. Phys. Lett.* **2012**, *100* (9), 092905.
(33) Hong, L.; Wu, P.; Li, Y.; Gopalan, V.; Eom, C.; Schlom, D.; Chen, L. *Phys. Rev. B: Condens. Matter Mater. Phys.* **2014**, *90* (17), 174111.
(34) Wang, J.; Ma, X.; Li, Q.; Britson, J.; Chen, L. *Acta Mater.* **2013**, *61* (20), 7591.
(35) Haun, M.; Furman, E.; Jang, S.; McKinstry, H.; Cross, L. *J. Appl. Phys.* **1987**, *62*, 3331−3338.
(36) Sheng, G.; Li, Y.; Zhang, J.; Choudhury, S.; Jia, Q.; Gopalan, V.; Schlom, D.; Liu, Z.; Chen, L. *Appl. Phys. Lett.* **2010**, *96*, 232902.
(37) Chen, Z.; Damodaran, A.; Xu, R.; Lee, S.; Martin, L. *Appl. Phys. Lett.* **2014**, *104*, 182908.
(38) Uecker, R.; Velickov, B.; Klimm, D.; Bertram, R.; Bernhagen, M.; Rabe, M.; Albrecht, M.; Fornari, R.; Schlom, D. *J. Cryst. Growth* **2008**, *310* (10), 2649−2658.
(39) Tagantsev, A. *Ferroelectrics* **2008**, *375*, 19−27.
(40) Ivry, Y.; Chu, D.; Scott, J.; Durkan, C. *Phys. Rev. Lett.* **2010**, *104* (20), 207602.
(41) Jia, C.; Urban, K.; Alexe, M.; Hesse, D.; Vrejoiu, I. *Science* **2011**, *331*, 1420−1423.
(42) Nelson, C.; Winchester, B.; Zhang, Y.; Kim, S.; Melville, A.; Adamo, C.; Folkman, C.; Baek, S.; Eom, C.; Schlom, D.; Chen, L.; Pan, X. *Nano Lett.* **2011**, *11* (2), 828−834.

(43) Luk'yanchuk, I.; Lahoche, L.; Sene, A. *Phys. Rev. Lett.* **2009**, *102*, 147601.

(44) Stephanovich, V.; Luk'yanchuk, I.; Karkut, M. *Phys. Rev. Lett.* **2005**, *94*, 047601.

(45) Levanyuk, A.; Misirlioglu, I. *J. Appl. Phys.* **2016**, *119*, 024109.

(46) Gu, Y.; Rabe, K.; Bousquet, E.; Gopalan, V.; Chen, L. *Phys. Rev. B: Condens. Matter Mater. Phys.* **2012**, *85*, 064117.

(47) Zhou, Z.; Wu, D. *AIP Adv.* **2015**, *5*, 107206.

(48) Stepkova, V.; Marton, P.; Setter, N.; Hlinka, J. *Phys. Rev. B: Condens. Matter Mater. Phys.* **2014**, *89*, 060101.

(49) Gui, Z.; Wang, L.; Bellaiche, L. *Nano Lett.* **2015**, *15*, 3224−3229.

(50) Marton, P.; Rychetsky, I.; Hlinka, J. *Phys. Rev. B: Condens. Matter Mater. Phys.* **2010**, *81*, 144125.

(51) Ren, W.; Bellaiche, L. *Phys. Rev. Lett.* **2011**, *107*, 127202.

(52) Wang, Y.; Nelson, C.; Melville, A.; Winchester, B.; Shang, S.; Liu, Z.; Schlom, D.; Pan, X.; Chen, L. *Phys. Rev. Lett.* **2013**, *110*, 267601.

(53) Lukyanchuk, I.; Sharma, P.; Nakajima, T.; Okamura, S.; Scott, J.; Gruverman, A. *Nano Lett.* **2014**, *14*, 6931−6935.

(54) Qiu, Q.; Nagarajan, V.; Alpay, S. *Phys. Rev. B: Condens. Matter Mater. Phys.* **2008**, *78*, 064117.

(55) Lee, D.; Lu, H.; Gu, Y.; Choi, S.; Li, S.; Ryu, S.; Paudel, T.; Song, K.; Mikheev, E.; Lee, S.; Stemmer, S.; Tenne, D.; Oh, S.; Tsymbal, E.; Wu, X.; Chen, L.; Gruverman, A.; Eom, C. *Science* **2015**, *349*, 1314−1317.

(56) Peters, J.; Apachitei, G.; Beanland, R.; Alexe, M.; Sanchez, A. *Nat. Commun.* **2016**, *7*, 13484.